ELSEVIER ELSEVIER

Contents lists available at ScienceDirect

Journal of Catalysis

journal homepage: www.elsevier.com/locate/jcat



An analysis of electroless deposition derived Ni-Pt catalysts for the dry reforming of methane



Benjamin T. Egelske ¹, Jayson M. Keels ¹, John R. Monnier, John R. Regalbuto *

University of South Carolina, Columbia, United States

ARTICLE INFO

Article history:
Received 23 July 2019
Revised 26 October 2019
Accepted 29 October 2019
Available online 2 December 2019

Keywords: Dry reforming Electroless deposition Nickel-platinum Kinetics Compensation effect

ABSTRACT

A series of nickel-platinum catalysts supported on gamma alumina (γ -Al₂O₃) with small, increasing amounts of Pt promoter were precisely prepared by electroless deposition at 5.0 wt% Ni and with compositions up to 2.8 wt% Pt (one theoretical monolayer of Pt on Ni) and evaluated for the dry reforming of methane. Characterization was performed using x-ray diffraction, temperature programmed reduction, scanning transmission electron microscopy, and temperature programmed oxidation. At temperatures below 600 °C, activity of bimetallic samples exhibited a maximum at 0.4 monolayers Pt and surpassed that of unpromoted Ni. At 700 °C, deactivation occurred for all samples. X-ray diffraction patterns of the high-temperature treated catalysts indicated segregation of the Ni-Pt alloys. Pt showed no influence on hydrogen selectivity, which was driven by thermodynamic limits.

© 2019 Elsevier Inc. All rights reserved.

1. Introduction

Traditionally generated through catalytic steam methane reforming (SMR), syngas (CO and H₂) is a fundamental building block for many industrial processes. In SMR, water (H₂O) acts as an oxidant in the reaction with hydrocarbon fragments to form hydrogen (H₂) and carbon monoxide (CO). As H₂ applications expand and more stringent carbon emission policies are put into effect, there is a growing incentive to find alternative H₂ sources as well as applications for CO₂ and CH₄ [1-3]. One possibility is the dry reforming of methane (DRM), in which CO₂ replaces H₂O as an oxidant. Depending on market conditions, downstream syngas can be further processed with in place technologies to satisfy a diverse chemical portfolio through methanol chemistry or C1 upgrading. In a recent paper by Elbashir et al. carbon footprint was analyzed as a function of syngas ratio (H₂/CO) for different reforming technologies [4]. It was concluded that DRM could result in a net fixation of CO₂ for product ratios approaching 1 to 1 and that additional processing, such as integration with exiting syngas technology, could increase H₂ levels but would also incur a penalty for CO₂ emissions.

Transition metals, specifically those of group VIII-B, have shown high DRM activity but economic feasibility has resulted in an

emphasis on Ni catalysts. Although active, widespread commercialization of a Ni-based DRM process is prevented by rapid deactivation from coke formation. Previous studies have shown that the introduction of an additional noble metal leads to increased activity as well as stability and in this study Pt was chosen for its widely reported synergistic effects [5–7]. Specifically, increased activity is often attributed to Pt assisted reduction of the NiO which promotes the formation of surface hydroxyls increasing the rate of carbon gasification [8,9]. Improved stability is commonly cited to result from a reduction of the Ni ensemble size which slows the rate of complete CH₄ decomposition to coke by disfavoring the tetrahedral structure for adsorbed CH_x species [6,10]. Furthermore, due to a reduction of the carbon-metal bond strength and lattice diffusivity noble metals have also been shown to inhibit whisker carbon formation which can lead to mechanical degradation in structured supports [11,12].

While literature has previously reported positive bimetallic effects for DRM, many studies utilized traditional impregnation methods for catalyst preparation [13]. Although simple, conventional impregnation randomizes metal-metal contact making it difficult to isolate bimetallic effects and limits the degree to which interactions can be optimized. Advanced techniques, such as atomic layer deposition (ALD), have shown promise for improved lab scale performance but commercial feasibility is mitigated by high waste to product ratios and a large energy demand during catalyst synthesis [5,14,15]. In addition, many previous Ni-Pt studies were performed across a narrow range of evaluation temperatures which can overlook the operating limits for material performance

^{*} Corresponding author at: College of Engineering and Computing, Horizon I Engineering Center, Office 018, 541 Main Street, Columbia, SC 29208, United States. E-mail address: REGALBU]@cec.sc.edu (J.R. Regalbuto).

¹ Co-first authors.

[5,8,16]. To address these challenges, the current study utilizes the synthesis technique of electroless deposition (ED), with which Pt atoms can be placed directly onto the supported Ni nanoparticles in controlled amounts, allowing for the first time the determination of an optimum Pt loading. Furthermore, performance has been evaluated in low and high (525–700 °C) temperature regimes which has revealed the source of catalyst instability at the high temperature.

2. Experimental

2.1. Synthesis

5.0 wt% Ni and 3 wt% Pt monometallic catalysts were prepared by dry impregnation (DI) of Ni(NO₃)₂ (Alfa Aesar) and H₂PtCl₆ (Sigma Aldrich) onto γ -Al₂O₃ (SBa 200, Sasol, 189 m² g⁻¹ specific surface area, 0.76 m³ g⁻¹ pore volume) respectively. Samples were dried in air at room temperature overnight, followed by a 265 SCCM He treatment at 100 °C for 12 h (superficial velocity = 12 c m/min), and reduced in-situ at 600 °C for Ni and 200 °C for Pt under 30% H₂/He for 2 h. The 5.0 wt% Ni/ γ -Al₂O₃ sample served as the base catalyst for electroless deposition (ED) with varying amounts of theoretical monolayers Pt, Table 1. The Ni-Pt catalysts are referred to as Ni@nPt where n is the number of theoretical monolayers calculated from the amount of surface Ni atoms, approximated using the STEM derived number average of 6.0 nm.

The ED bath, previously developed [17], consisted of H_2PtCl_6 as the Pt precursor, dimethylamine borane (DMAB) as the reducing agent, and ethylene diamine (EN) as a chelating agent. The DMAB/EN/Pt molar ratio was held constant at 5/4/1 while varying the initial absolute Pt concentration in order to achieve the desired Pt coverage. The ED bath was heated to $70\,^{\circ}$ C under constant stirring before the Ni/ γ -Al $_2$ O $_3$ catalyst was added. NaOH was added to maintain a pH value of \sim 11. Aliquots were taken to monitor Pt concentration using inductively coupled plasma optical emission spectroscopy (ICP, Perkin Elmer Optima 2000 DV). After complete deposition (30 min), catalysts were filtered and washed with 1 L/g catalyst deionized water to remove byproducts and unreacted components. All bimetallic catalysts were dried at room temperature in air overnight then heat treated in 30% H_2 balance He at $200\,^{\circ}$ C for 2 h.

2.2. Characterization

Temperature program reduction (TPR) studies were conducted in a Micrometrics Autochem II 2920 equipped with a thermal conductivity detector (TCD). Temperature programed oxidation (TPO) was performed using a quartz tube furnace connected to an Inficon Transpector 2 Mass Spectrometer. TPR samples were oxidized at 300 °C for 2 h under a flow of 10% O_2 balance He, then cooled to room temperature in flowing Argon (Ar). The flow was then switched to 20 SCCM of 10% H_2/Ar and outlet gases were monitored using a TCD. The TCD signal was allowed to stabilize before

the sample was ramped to 800 °C at a rate of 10 °C/min. TPO samples were loaded into a 1/4-inch quartz tube (4 mm ID) supported on a quartz wool plug and placed inside a high wattage, split-tube furnace. The sample was then heated from 25 to 800 °C at 10 °C/min under a 20 SCCM flow of 10% O_2 /He. Relative amounts of coke were determined by integrating the normalized signal for CO_2 (m/e = 44), which was calibrated after each run.

A Rigaku Miniflex Series II diffractometer equipped with a D/teX silicon strip detector and CuKα1 radiation was used for powder x-ray diffraction (XRD). Previous experiments have shown a negligible effect from instrument line broadening for the equipment used in this study [18]. Scans were performed over a 2θ range of 10–80° with a scan speed of 1°/min and sampling width of 0.02°. XRD results were correlated with scanning transmission electron microscopy (STEM) images captured using a cold field emission, probeaberration-corrected, 200 kV JEOL JEM-ARM200CF. The microscope is fitted with JEOL and Gatan detectors for acquiring high-angle annular dark field (HAADF) images. X-ray energy dispersive spectroscopy (XEDS) was also employed using an Oxford Instruments X-Max100TLE SDD detector and analyzed with Oxford AZtec software.

2.3. Catalytic testing

Reaction studies were performed in a continuous flow quartz tube, 4 mm ID, heated with a split tube high temperature furnace (Applied Test Systems, Series 3210). Upstream, gas ratios were regulated using Brooks 5850E mass flow controllers and mixed inline before reaching the reactor. Product streams were heated to 150 °C to avoid condensation and sampled at automated 1 h intervals using an HP 5890 Series II gas chromatograph (GC) equipped with two TCDs. TCD 1 was referenced with He gas (Praxair, HE5.0UH) and uses a PoraPLOT Q (Agilent) column to detect carbon compounds (CO,CO₂,CH₄) and H₂O. TCD 2 uses an Ar reference (Praxair,

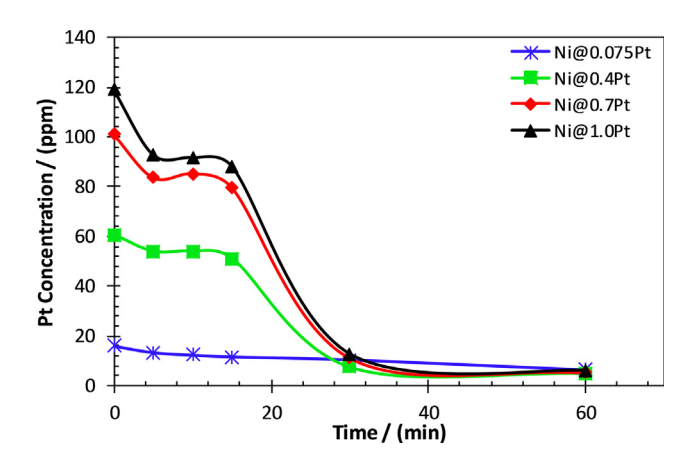


Fig. 1. Platinum uptake vs time for electroless deposition. A shelf is formed at t = 10 min where NiO is reduced by DMAB.

Table 1Bulk atomic % loadings and calculated Ni/Pt atomic ratios for monometallic Ni and bimetallic Ni-Pt ED catalysts. Catalyst ID's are referred to as Ni@nPt where n is the number of theoretical monolayers calculated from STEM derived number averages.

Catalyst ID	Weight % Ni	Weight % Pt	Atomic % Ni	Atomic % Pt	Ni/Pt atomic ratio
Ni /γ-Al ₂ O ₃	5.0	0	100	0	=
Ni@0.075Pt	5.0	0.2	98.8	1.2	82.3
Ni@0.4Pt	5.0	1.1	93.8	6.2	15.3
Ni@0.7Pt	5.0	1.9	89.8	10.2	8.8
Ni@1.0Pt	5.0	2.8	85.8	14.2	6.0
Pt $/\gamma$ -Al ₂ O ₃	0	3	0	100	0

UHP, 5.0) and a Carboxen 1010 PLOT (Supelco) column to capture H_2 data.

For high temperature evaluation, reactors were loaded with 0.01 g of catalyst diluted with 0.06 g 20/40 mesh crushed quartz such that bed height was 2X reactor ID. Samples were ramped to 600 °C at a 10 °C/min ramp rate in flowing H_2 , soaked for 2 h, then increased to a reaction temperature of 700 °C in He. The feed composition consisted of a CH_4 (Praxair, ME3.7UH)/ CO_2 (Praxair,

Research Grade, 4.8)/He (Praxair, HE5.0UH) ratio of 1/1/2 while GHSV varied from 33,000 to 49,500 h⁻¹ to avoid external diffusion resistance reported by Mark and Maier [19] and set initial CH₄ conversions between 30 and 50%. After reaching *pseudo steady state*, defined as 3 consecutive hours at constant CH₄ conversion, GHSV was adjusted to reach 19,000 h⁻¹ and approximately 40% CH₄ conversion providing a common reference to study deactivation kinetics far from thermodynamic equilibrium (85% CH₄ conversion).

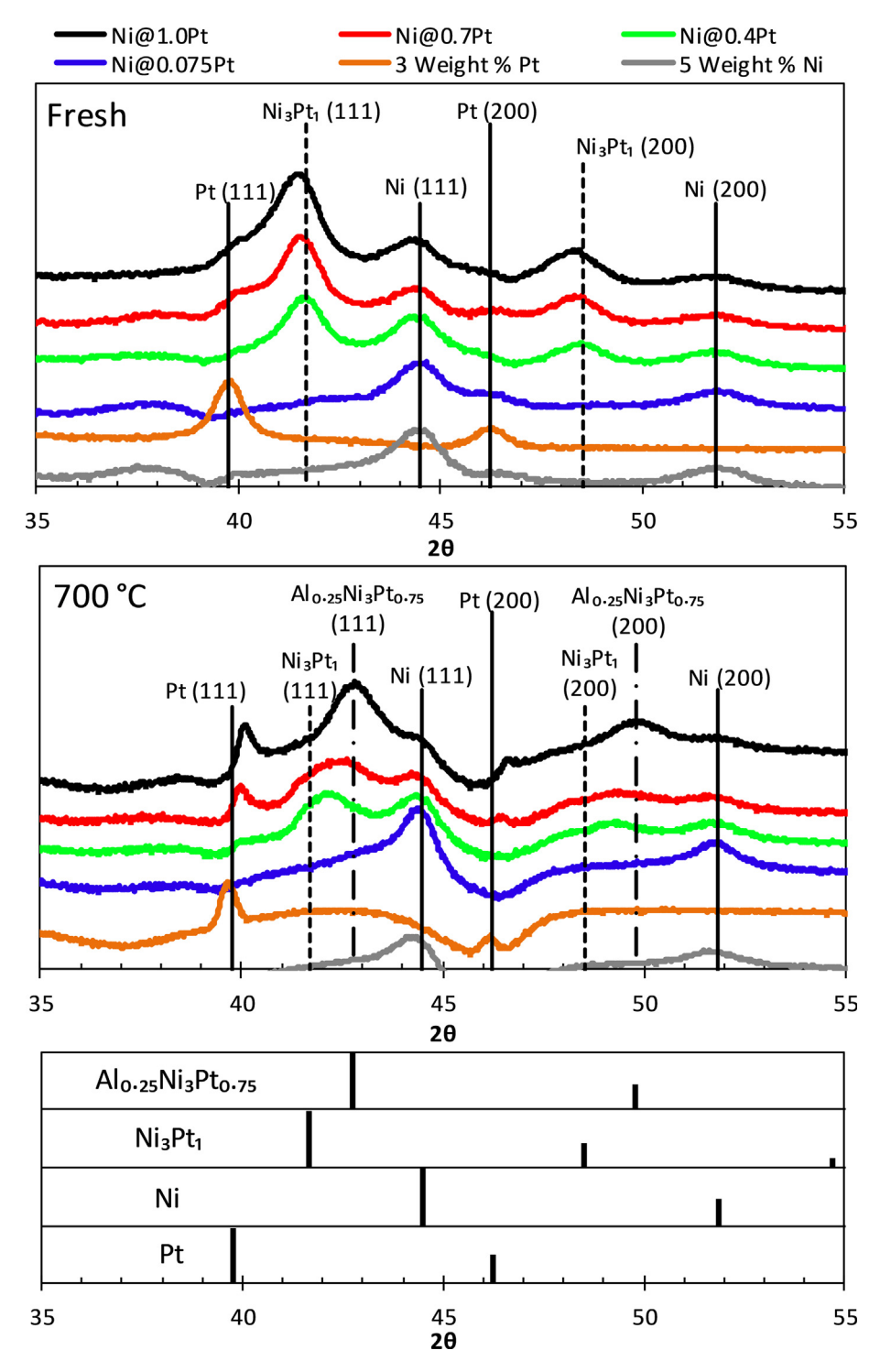


Fig. 2. (Top) Fresh samples after an ex-situ reduction in H₂ at 200 °C note the appearance of an alloy peak with the addition of Pt. (Middle) Spent samples after exposure to DRM at 700 °C for 20 h. After reaction all alloy and Pt peak intensities decrease and increase respectively. (Bottom) Reference patterns.

Calculated Weisz-Prater numbers at 19,000 h^{-1} GHSV for CH₄ (0.018) and CO₂ (0.018) suggest the absence of pore diffusion effects over the region of linear deactivation (TOS 20–80 h). Selectivity was defined according to Eqs. (1) and (2) where N_x represents the moles of gas x and a, b, c, and d are stoichiometric coefficients

$$aCH_4 + bCO_2 \leftrightarrow cCO + dH_2$$
 (1)

$$Sc = \frac{(N_{H_2Produced})(d)}{(N_{CH_4Consumed})(a)} * 100\%$$
(2)

Kinetic evaluations used 0.01 g of catalysis diluted with 0.06 g 20/40 mesh crushed quartz and reduced at 700 °C using the protocol noted above. All experiments were performed below 10% CH₄ conversion to avoid mass transfer and thermodynamic limitations. Reactions were brought online at 550 °C with a $\rm CH_4/CO_2/He$ ratio of

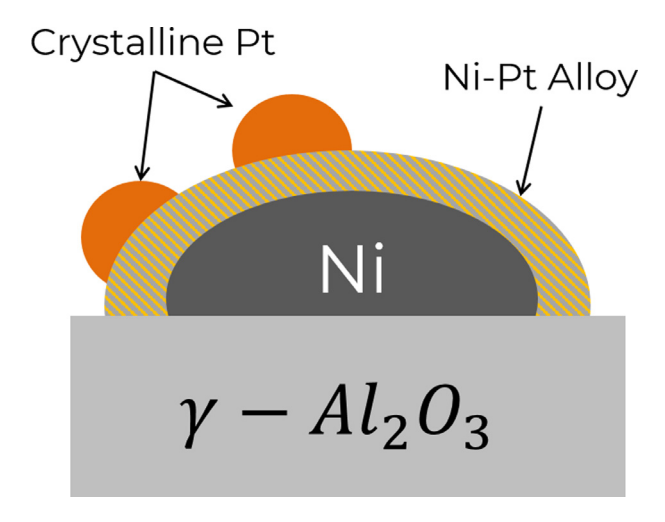


Fig. 3. Proposed structure for electroless deposition derived Ni-Pt samples following reduction in $\rm H_2$ at 200 °C.

1/1/2 until pseudo steady state was obtained at which point temperature was reduced to 525 °C and flow rates adjusted to maintain measurable CH₄ conversion rates while keeping partial pressures constant. Upon reaching the new pseudo steady state, this procedure was repeated for 575, 600, 550, 600 and 625 °C to verify reversibility and repeatability. Once determined, flow rates at each temperature were held constant for all catalysts in Table 1. Calculated Weisz-Prater numbers for kinetic evaluations were approximately zero for CH₄ and CO₂. All thermodynamic calculations were performed using Aspen HYSYS (V10, 36.0.0.249) though a minimization of Gibbs free energy with the Peng-Robinson model.

3. Results & discussion

3.1. Preparation

Following reduction of the DI 5.0 wt% Ni catalyst, samples were exposed to air before electroless deposition was used to synthesize the Ni-Pt series in Table 1. Pt uptake onto 5.0 wt% Ni/ γ -Al₂O₃ is shown as a time dependent concentration profile with 4 distinct regions, Fig. 1. At time 0 to 5 min (1) initial Pt uptake on easily reduced NiO occurs until a plateau is reached between 5 and 15 min (2). This plateau is attributed to NiO formed during storage in air, which required additional time to undergo reduction by DMAB. The appearance of NiO in the XRD patterns of fresh catalysts (Fig. 2 Fresh), is seen most clearly as the broad NiO (101) peak centered at 37.3° 20 and the NiO (012) peak at 43.3° 20 (JCPDS: 00-044-1159). Seen most clearly for the Pt-free sample, these peaks diminish with increasing Pt content. In the ED bath after the NiO is reduced, rapid Pt uptake occurs between 15 and 30 min (3) after which no additional deposition occurs. This final plateau (4) was thought to arise due to low Pt concentrations, 5–6 ppm, where deposition is no longer favored [17].

XRD patterns after ex-situ reduction, noted above as fresh in Fig. 2, exhibit prominent Ni (111) peaks at 44.5° 2θ (JCPDS: 01-071-3740) for all measured Pt loadings and Pt (111) peaks at 39.8° 2θ (JCPDS: 01-070-2431) for 0.7 and 1.0 monolayer samples. Between the Pt (111) and Ni (111) peak a strong Ni-Pt alloy peak

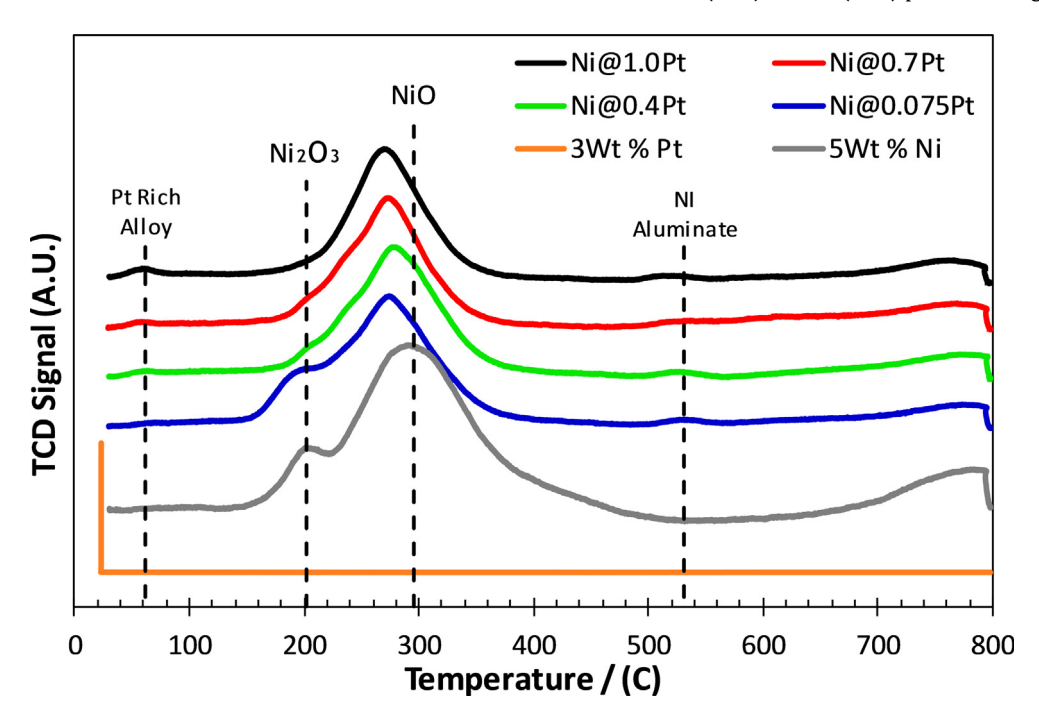


Fig. 4. TPR results indicating a decrease in Ni reduction temperature at 300 °C. Note the formation of an additional low temperature peak at 50 °C attributed to a Pt rich alloy and high temperature peak at 530 °C likely the formation of Ni aluminates.

with an approximate 3 to 1 Ni/Pt ratio was observed (JCPDS: 01-074-6872). To obtain clean diffraction patterns the $\gamma\text{-Al}_2O_3$ support was deconvoluted from the metallic peaks by first normalizing all signals 0 to 1 then subtracting an unmodified $\gamma\text{-Al}_2O_3$ from the metal-support profile. A complete procedure for normalization and peak subtraction can be found in the supplementary material. The presence of a Ni-Pt alloy accompanied by a crystalline Pt peak suggests autocatalytic deposition of Pt salt onto reduced Pt metal during ED to form measurable Pt ensembles, as depicted in Fig. 3. The presence of NiO in the fresh samples was noted above. Additional

EDX imaging, included in the supplementary material, showed no evidence for Pt deposition on the γ -Al $_2$ O $_3$ support and bath stability experiments showed no uptake from strong electrostatic interactions or thermal decomposition of the Pt precursor.

TPR of pre-oxidized samples was used to confirm the proximity of Pt to the Ni phase; results are shown in Fig. 4. A pure Pt sample exhibits a sharp peak at the 23 °C. The Pt-free Ni sample shows a main reduction peak at 295 °C and a small shoulder peak at 200 °C previously associated with Ni³⁺ in the form of Ni₂O₃ [20]. As the ED-deposited Pt loading increases, the temperature of the

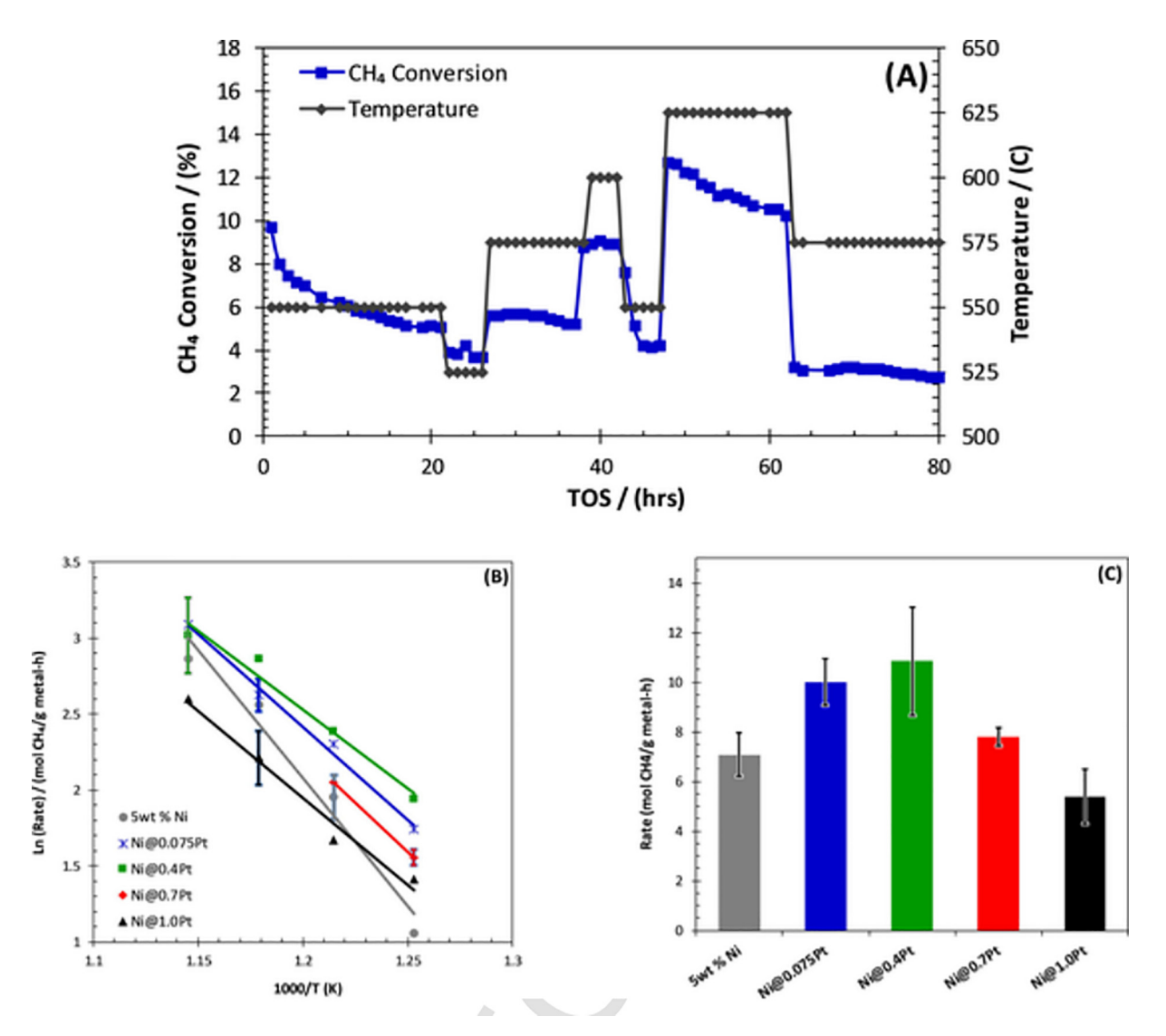


Fig. 5. (A) Representative kinetic runtime data taken for Ni@0.075Pt. (B) Arrhenius plots for catalysts in Table 1 at temperatures between 525 and 600 °C. Error bars represent triplicate data captured at 550 °C for each sample and plotted at higher temperatures for readability. (C) Steady state CH₄ conversion rates at 550 °C. At 600 °C, thermodynamic equilibrium is near 50% CH₄ conversion.

Table 2 Arrhenius data for ED derived Ni-Pt catalysts captured between 525 and 600 $^{\circ}\text{C}.$

Catalyst	Atomic % Ni	Atomic % Pt	Ea' (KJ/mol)	Ln(A')
5 wt% Ni	100	-	122.2 ± 6.6 ^a	19.7 ± 3.2 ^a
Ni@0.075Pt	98.8	1.2	101.5 ± 3.9 ^a	16.6 ± 2.3 ^a
Ni@0.4Pt	93.8	6.2	86.2 ± 2.9^{a}	15.0 ± 5.5 ^a
Ni@0.7Pt	89.8	10.2	95.8 ± 1.5 ^a	16.0 ± 1.9 ^a
Ni@1.0Pt	85.8	14.2	96.4 ± 3.45^{a}	15.8 ± 4.0 ^a
3 wt% Pt	-	100	-	-

a Error propagated from triplicate rate data collected at 550 °C assuming relatively constant uncertainty with increasing temperature.

main reduction peak decreases, consistent with lower reduction temperatures of Ni-Pt alloys seen in previous studies [5,8,21]. A maximum offset of 30 °C is observed for a loading of one monolayer of Pt. The reduction of both the Ni and Ni₃Pt phases seen in the XRD patterns of the fresh catalysts (Fig. 2) would occur in the main peak. The low temperature shoulder at 200 °C on the Ni-only catalysts diminishes as the Pt loading increases; this suggests that since Pt does not oxidize below 300 °C [23–25], that Pt at the Ni surface stabilizes the surface against oxidation to Ni³⁺. The appearance of a small, low temperature (50 °C) peak at the higher Pt loadings is consistent of the XRD observation (Fig. 2 Fresh) of small amounts of a Pt rich alloy at the higher Pt loadings, and the small high temperature peaks at 530 °C are likely due to Pt assisted reduction of Ni aluminates [22].

3.2. Low temperature kinetics

Kinetic evaluations were performed at constant partial pressures and $\rm CH_4$ conversions below 10% to avoid mass transfer and thermodynamic limitations. At temperatures exceeding 600 °C, deactivation was observed for both monometallic and bimetallic samples limiting the conditions at which kinetic data could be obtained, Fig. 5A (50 h TOS). Therefore, Arrhenius data is reported up to 550 °C for 0.7 theoretical monolayers Pt and 600 °C for all other catalysts, Fig. 5B.

Kinetic results indicate a synergistic effect for Ni-Pt systems. Assuming a general rate expression, Eq. (3), and Arrhenius behavior, Eq. (4), apparent activation energies were calculated for the Ni-Pt series, Table 2. Where k_0 is the rate constant, P_x is the partial pressure of reactant x, α and β are reaction orders, A_0' is the apparent pre-exponential factor, E_a' is the apparent activation energy, R is the ideal gas constant, and T is the reaction temperature in Kelvin.

$$Rate_{CH_4Consumption} = (k_0)(P_{CH_4}^{\alpha})(P_{CO_2}^{\beta})$$
(3)

$$k_0 = (A_0')e^{(-\frac{E_0'}{RI})}$$
 (4)

while it is traditionally hazardous to infer mechanistic information based solely on apparent activations energies, the conditions used in this study (525–600 °C, 101 kPa, 1/1/2 CH₄/CO₂/He Feed) suggest a first order dependence on CH₄ [26,27]. Therefore, above 525 °C it was assumed that CH₄ surface coverages were negligible and under these conditions CH₄ activation was approximated to be the sole rate determining step [27,28]. From the Arrhenius data, calculated apparent activation energies for all samples agree with those previously reported for DRM (92, 96, and 109 kJ/mol on Ni/MgO, Ni/SiO₂ and Ni/TiO₂) but a comparison of the monometallic and bimetallic data showed a consistent reduction in activation energy for the Ni-Pt series, Fig. 5B [6,29–31]. Since Pt is known to assist dehydrogenation, it is likely lowering the CH₄ decomposition barrier and improving rates for low to moderate Pt coverages between 525 and 600 °C, Fig. 5B and C [32,33].

Extending the analysis to a review of CO adsorption enthalpies at 0.2 monolayers for Ni(100) (135 kJ/mol) and Pt(111) (115 kJ/mol) suggests a negligible inhibition from product species, but a comparison of temperature programed desorption (TPD) patterns for Ni, Pt, and Ni-Pt ALD samples indicates a drastic increase in the CO desorption temperature (+300 °C) for bimetallic samples [5,34–36]. In separate studies, Gould et al. compared a series of incipient wetness prepared Ni/Al₂O₃ to Ni-Pt/Al₂O₃ ALD samples and demonstrated a broad CO desorption peak (100–400 °C) for Ni and a narrow high temperature peak (400–625 °C) for bimetallic samples [37]. Furthermore, peak areas were shown to scale with increasing numbers of ALD cycles suggesting a correlation between Pt loading and CO capacity. This result could explain why in the present study, low Pt loadings (0.4 & 0.075 ML) out performed higher loadings (0.7 & 1.0 ML) at 550 °C, Fig. 5B.

3.3. High temperature evaluation

High temperature experiments were performed at 700 °C with CH₄ conversions between 35% and 45% providing sufficient load to test deactivation kinetics absent thermodynamic equilibrium at approximately 85% conversion. Between 0 and 20 h, samples were allowed to reach *pseudo steady state* before flow rates were adjusted to a constant GHSV (19000 h⁻¹) while maintaining partial pressures. Two observations were apparent from the high temperature data in Fig. 6. First, after reaching a GHSV of 19,000 h⁻¹ linear

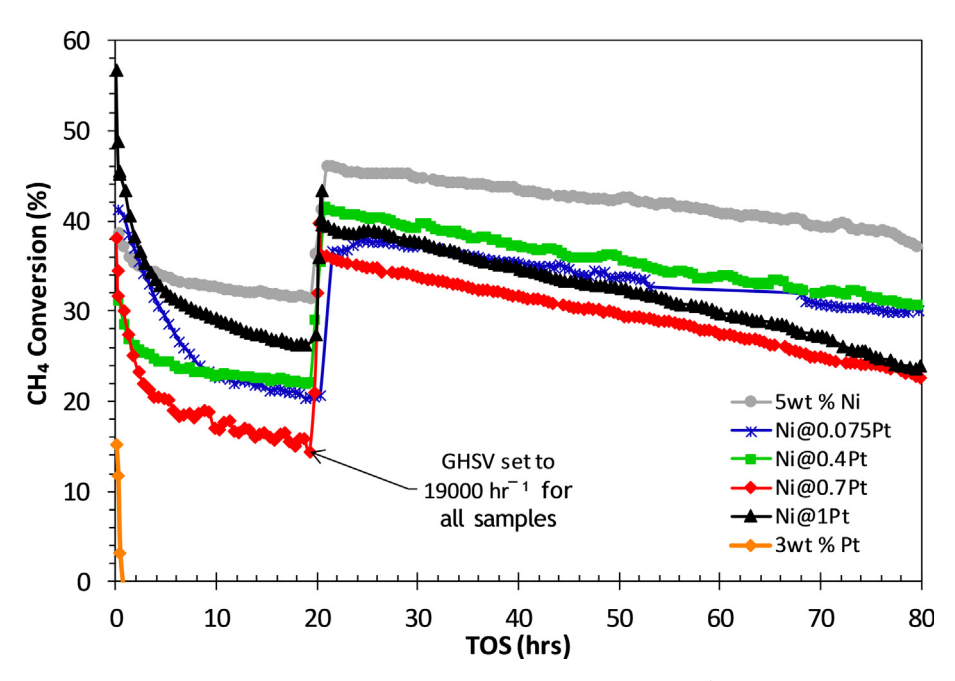


Fig. 6. Methane conversion at 700 °C as a function of time on stream with a common GHSV of 19,000 h^{-1} in excess of 20 h TOS. At 700 °C CH₄ conversion is thermodynamically limited at 85%.

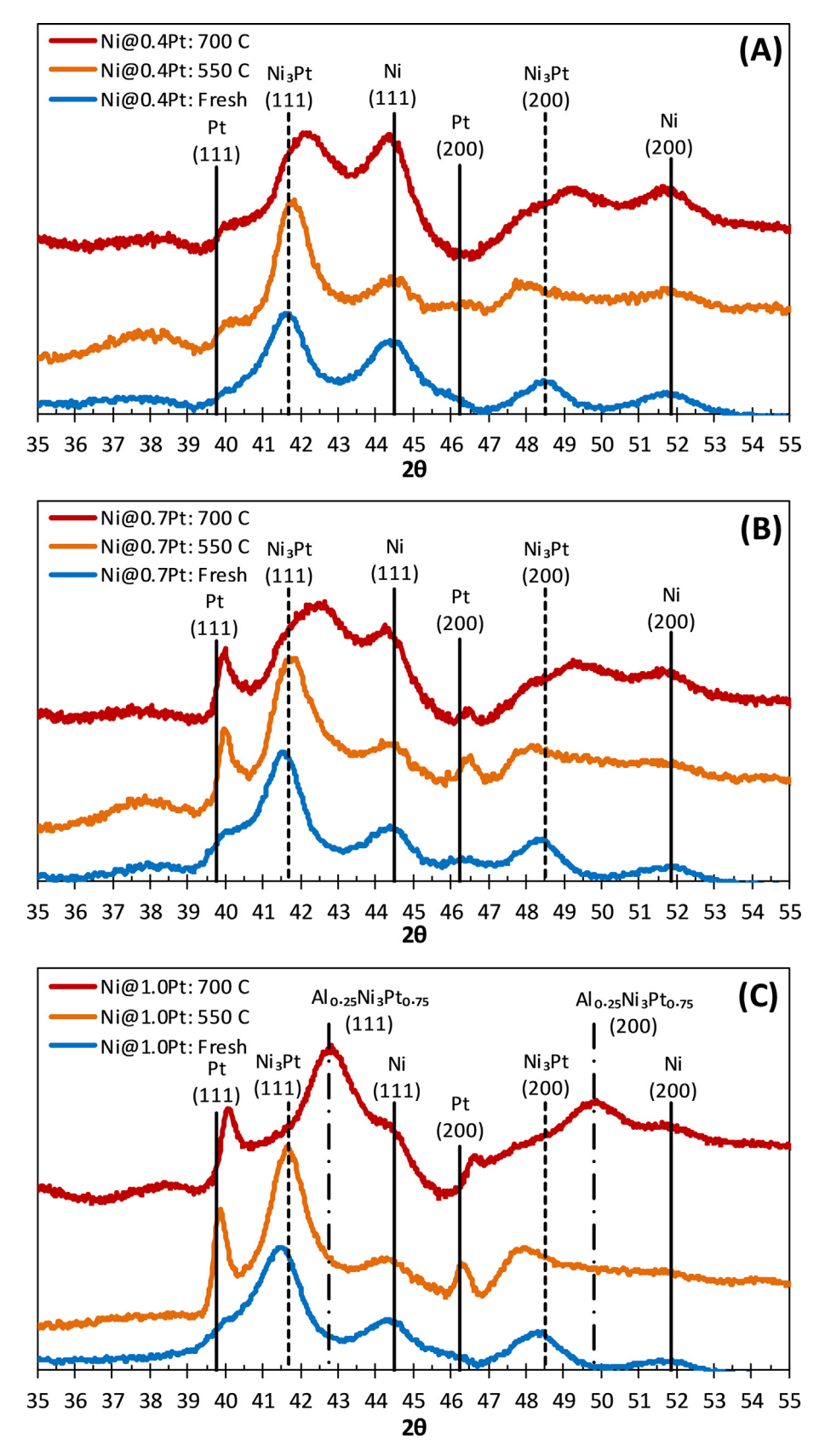
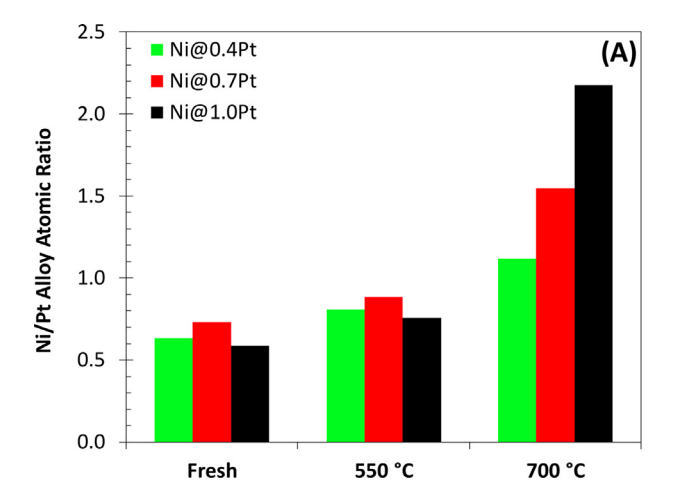


Fig. 7. XRD profiles for fresh samples reduced at 200 °C in H_2 , and spent samples treated under DRM conditions for 20 h at 550 and 700 °C for Ni@0.4Pt (A), Ni@0.7Pt (B), and Ni@1.0Pt (C).

deactivation was present for all samples. Second, all bimetallic catalysts showed lower activity compared to monometallic Ni. To explain this behavior a series of XRD, TPO and STEM experiments were performed. Fig. 2 compares XRD patterns for fresh samples, previously described in Section 3.1, and spent samples which were reduced in situ at 600 °C under H_2 and subjected to DRM for 20 h at 700 °C with a $CH_4/CO_2/He$ ratio of 1/1/2.

Spent samples in Fig. 2 show prominent Ni (111) peaks at 44.5° 20 for all measured Pt loadings and Pt (111) peaks at 39.8° 20 for 0.4, 0.7, and 1.0 monolayer samples. Between the Pt (111) and Ni (111) peak the Ni-Pt alloy peak shifts rightward for intermediate



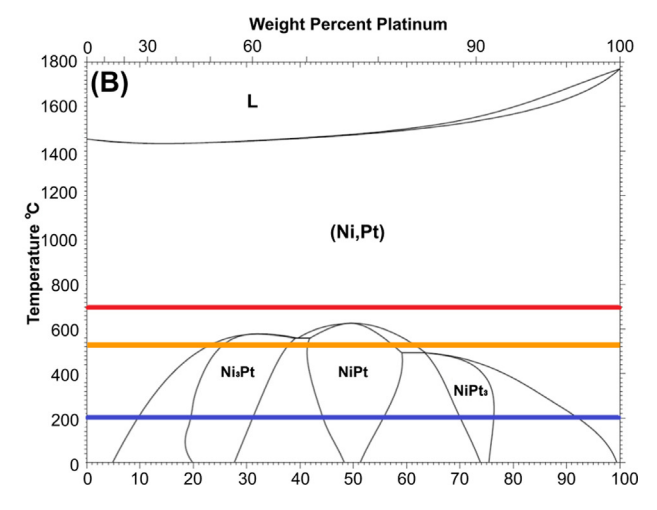


Fig. 8. (A) Ni/Pt atomic ratios calculated from Vegard's Law for fresh and spent catalysts after 20 h TOS at 550 and 700 °C. (B) Ni-Pt phase diagram post ED reduction temperature (Blue), high temperature XRD (Red), low temperature XRD (orange).

Pt loadings (0.4 & 0.7 ML) and a comparison to known XRD patterns for the 1.0 ML sample suggests the formation of a Ni-Pt-Al alloy (JCPDS: 01-071-5889) which may also explain differences in the fresh and spent baseline patterns.

In light of the findings for post reaction samples at 700 °C additional experiments were performed to probe surface reconstruction as a function of both temperature and composition, Fig. 7. Under DRM conditions at 550 °C, the Ni-Pt alloy peak remained fixed at 41.6° 20 and the intensity increased from 0.4 to 0.1 ML Pt. Furthermore, with additional Pt loading the metallic Ni (111) peak decreased and Pt (111) peak increased indicating growth of the Ni-Pt alloy phase. Applying Vegard's Law to the Ni₃Pt (111) peak, Eq. (5), where a_x is the pure metal or alloy lattice constant and X_{Pt} is the mole fraction of Pt, calculated Ni/Pt ratios suggest alloy stability at 550 °C but a Ni rich shift at 700 °C, Fig. 8A, and comparison of operating temperatures to the Ni-Pt phase diagram, Fig. 8B, predicts thermodynamic instability above 600 °C [38].

$$a_{Ni-Pt} = (1 - X_{Pt})(a_{Ni}) + (X_{Pt})(a_{Pt})$$
(5)

3.4. Ni-Pt stability

Ni-Pt alloy, metallic Ni, and metallic Pt particle sizes were calculated using the Scherrer Equation and displayed in Table 3. For pure metallic Ni and Pt, final values at 550 and 700 °C are nearly identical but compared with fresh samples, the final Ni, Pt, and Ni-Pt alloy showed a consistent increase in particle size. In addition, STEM experiments were performed for 5.0 wt% Ni, Ni@1.0Pt, Ni@0.7Pt, and Ni@0.4Pt and particle growth trends were in good agreement with XRD results but XEDS analysis also indicated a correlation between high Pt loadings and large Pt clusters for samples treated at 700 °C, Fig. 9. Furthermore, carbon whiskers were often associated with Pt loaded samples, an observation not found in the metallic Ni imaging. Without a large statistical dataset, it was difficult to make definitive conclusions regarding particle composition, size, or the degree of whisker carbon formation for fresh compared to spent samples. However, within this dataset there was sufficient evidence to suggest that the variability in DRM performance and particle composition was more prominent for Pt loadings greater than 0.4 monolayers, Fig. 9. Histograms for both fresh and spent Ni samples are included in the supplementary material and showed mean number averages of 6.0 ± 3.6 nm (n = 145) and 8.5 ± 2.7 nm (n = 101) respectively. Based on these measurements it was thought that deactivation due to sintering does not play a major role over the linear region (TOS 30-50 h) and instead, activity loss likely results from increased coke formation.

To quantify carbon deposition TPO was performed on select samples in which DRM was carried out at 700 $^{\circ}$ C until deactivation, then cooled in a He environment to release adsorbed hydrocarbons. Peaks shown in Fig. 10 (m/e = 44) were attributed to solid carbon burn-off and match temperatures previously reported [39]. The kinetic analysis in Section 3.2 showed an increase in

Table 3Ni, Ni-Pt Alloy, and Pt particle size calculated from XRD. Pt particle size increases by a factor of 3 for heat treated samples.

		Nickel		Ni-Pt Alloy		Platinum			
	Fresh	Spent (550)	Spent (700)	Fresh	Spent (550)	Spent (700)	Fresh	Spent (550)	Spent (700)
5 wt% Ni	4.6	=	5	=	=	-	=	-	=
Ni@0.075Pt	4.6	_	6.3	_	_	_	_	_	_
Ni@0.4Pt	4.5	5.7	6.2	6.9	7.4	5	7.6	_	_
Ni@0.7Pt	4.1	6.5	6.1	6.7	7.5	4.8	8.5	20.8	21
Ni@1.0Pt	4.7	6.2	6.4	7.25	8.1	5.8	7.8	27.8	21
3 wt% Pt	-	-	-	-	-	-	10.8	-	19.9

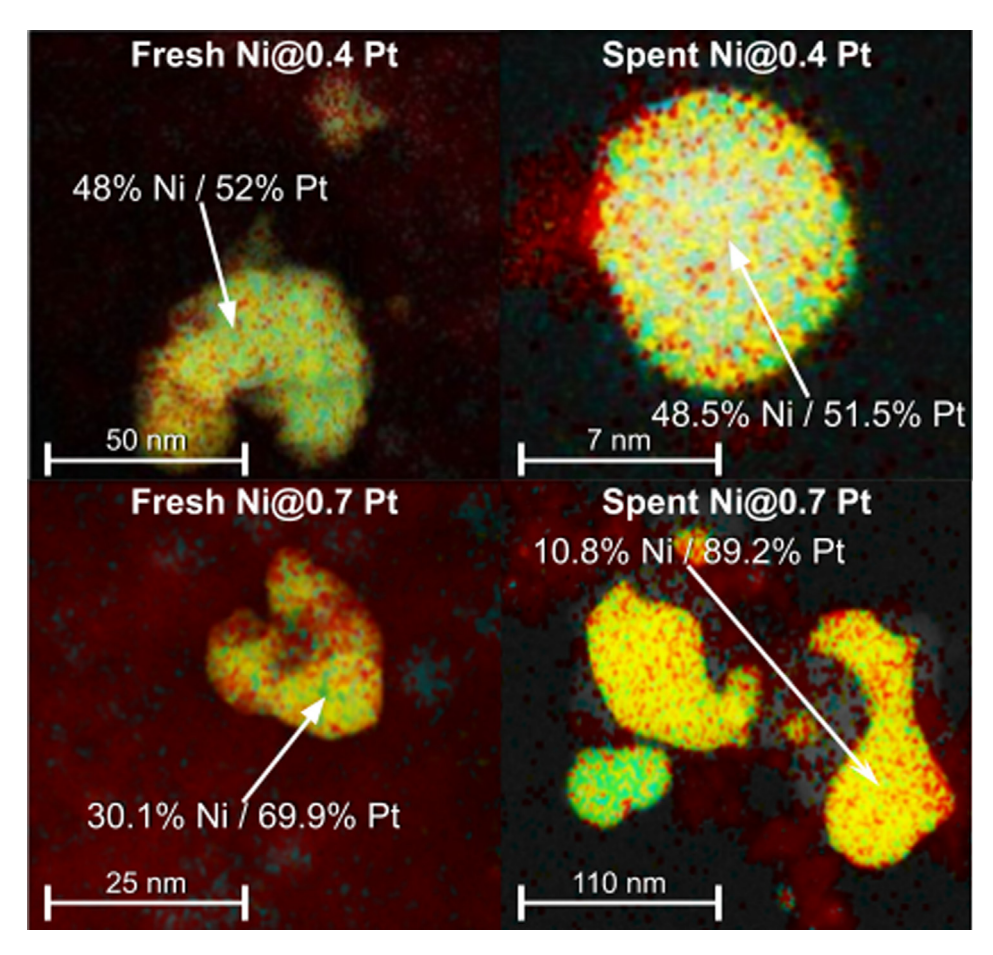


Fig. 9. EDX imaging for Pt agglomeration at high Pt atomic loading (Bottom) and stable alloy composition at low Pt atomic loading (Top). Gamma alumina support (Red), Pt (Yellow), Ni (Blue). Fresh samples have been reduced at 200 °C in H₂. Spent samples indicate exposure to DRM between 525 and 625 °C in excess of 50 h TOS.

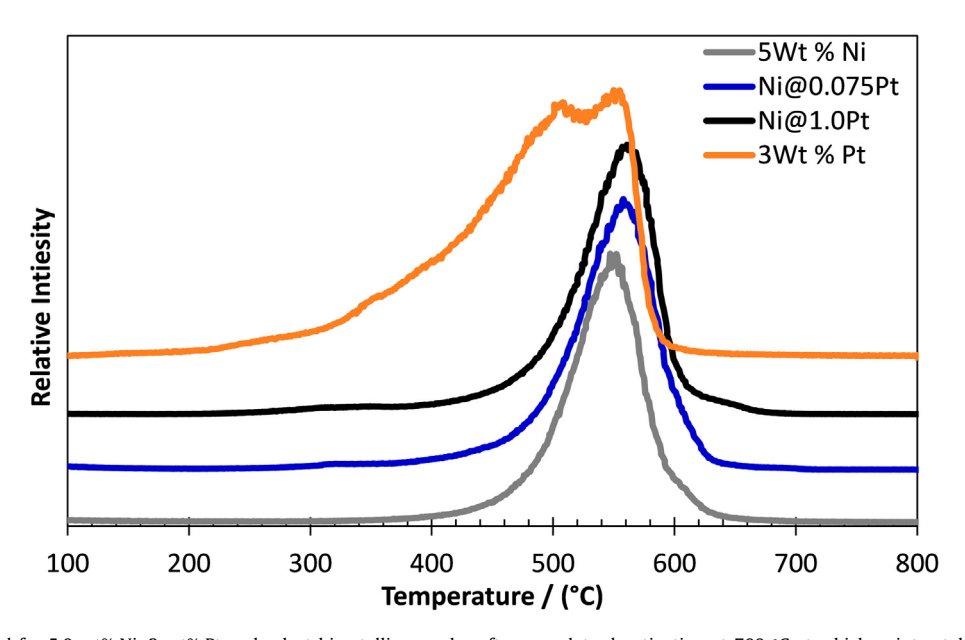


Fig. 10. TPO data collected for 5.0 wt% Ni, 3 wt% Pt and select bimetallic samples after complete deactivation at 700 °C at which point catalysts were cooled to room temperature in He to desorb residual hydorcarbons.

methane decomposition rates with the addition of Pt and the integrated m/e = 44 peak areas in Table 4 indicated a direct relationship between Pt loading and coke formation [21,22]. In agreement with the XRD results, TPO further suggested that

temperatures in excess of 600 °C favored separation of the Ni-Pt alloy to form large Pt ensembles which can over promote methane decomposition to surface carbon and increase catalyst deactivation rates over the linear region, Fig. 6 (TOS 30–50 h).

Table 4High temperature linear deactivation rates and integrated TPO peak areas (m/e = 44). Note peak integration was performed on spent samples after complete deactivation.

Catalyst	Ni/Pt atomic ratio	Deactivation rate (mmol CH ₄ h ⁻² g ⁻¹ _{metal}) ^b	Coke formation (mmol C/g _{cat})
5 wt% Ni	-	121.2	3.54 (150°)
Ni@0.075Pt	83.3	145.8	$4.22 (150^{\circ})$
Ni@0.4Pt	14.3	205.2	-
Ni@0.7Pt	8.8	242.1	-
Ni@1.0Pt	5.9	262.8	$6.99 (110^{\circ})$
3 wt% Pt	=	6774	7.21 (20°)

b Deactivation rate averaged over the linear region (30–50 h TOS), Fig. 4.

3.5. Ni-Pt activity

The high temperature results, Fig. 6, indicated an indirect correlation between Pt loading and activity with pure 5.0 wt% Ni outperforming all bimetallic samples. This inverse behavior was attributed to a compensation effect observed for this catalyst series [40–42].

$$\ln\left(A'\right) = \alpha + \frac{E_{a'}}{R\theta} \tag{6}$$

Eq. (6) describes the relationship between the apparent pre-exponential factor and apparent activation energy with α and θ representing a constant and the isokinetic temperature respectively. When plotted for the Ni-Pt series, a linear trend is formed with α = 3.14 and θ = 624 °C, Fig. 11. For a class of materials exceeding the isokinetic temperature, performance trends are expected to reverse i.e. the pre-exponential factor will increase with temperature to offset reduced apparent activation energies. This phenomenon explains why reaction rates are positively influenced by Pt addition below 600 °C, but negatively influenced at 700 °C and illustrates the importance of screening materials across a wide range of operating temperatures.

Since its first observation in 1925, many studies have sought to understand the nature of isokinetic compensation [41,43–46]. Due to the efforts of Exner, Linert, and Jameson [45,46] much of the early skepticism surrounding this phenomenon has been dissolved and physical significance is often accepted for the compensation relation, Fig. 11. However, we do not intend to apply chemical or catalytic significance to the meaning of this compensation effect, but to highlight the value of the isokinetic temperature, the temperature at which catalytic activities are the same for all the catalysts. The existence of an isokinetic temperature for a series of catalysts means activation energies are different and that a linear regression plot based on Eq. (6) will give the isokinetic temperature, 624 °C in this instance. As alluded above, comparisons of activities for a series of catalysts must be made for the same side of the isokinetic temperature. Thus, the order of activities will be different for each side, and the further away for the isokinetic temperature, the bigger the difference.

3.6. Ni-Pt selectivity

At conditions of similar conversion, high temperature selectivity showed no dependence on Pt loading. Further analysis under low temperature conditions, Fig. 12, agreed with thermodynamic predictions for H_2/CO ratios, typically 1 to 1 due to a strong reverse water gas shift reaction (RWGS) reaction, calculated from a minimization of Gibbs free energy. Under both conditions, a hydrogen balance (H_b) yielded values approaching unity for all samples

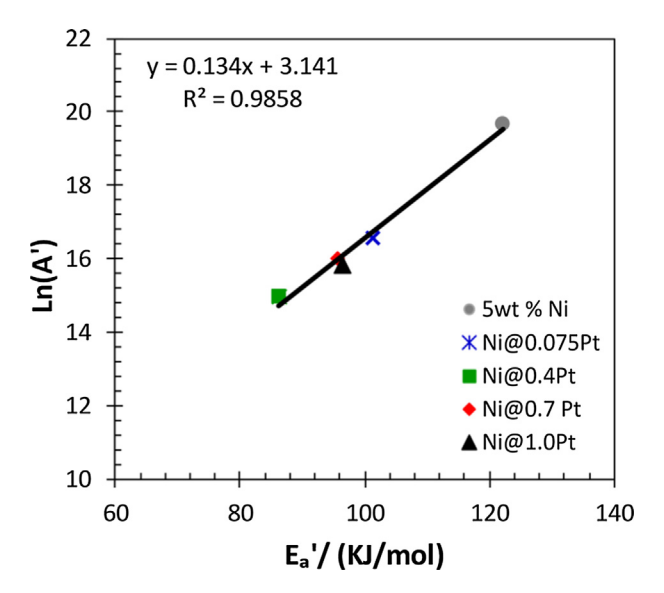


Fig. 11. Compensation plot for 5.0 wt% Ni (Gray), Ni@0.075Pt (Blue), Ni@0.7Pt (Red), Ni@1.0Pt (Black) and Ni@0.4Pt (Green) with an operating temperature between 525 and 600 $^{\circ}$ C.

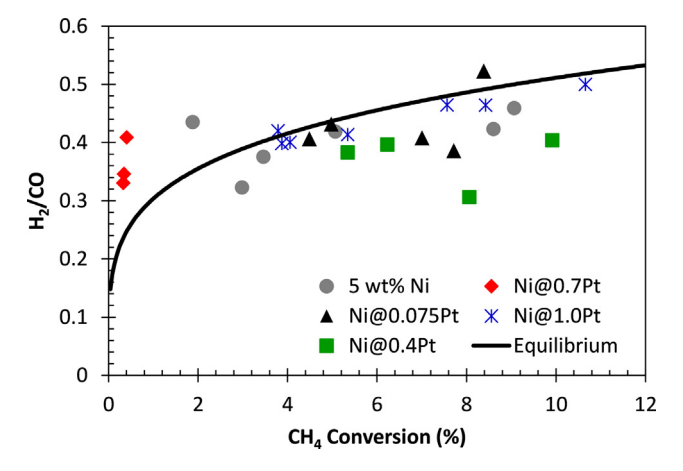


Fig. 12. H_2/CO ratios and the calculated thermodynamic limit (solid black) vs CH_4 conversion.

where N_x is the moles of each species, Eq. (7), which strongly suggests that Pt addition plays no role in H_2 selectivity.

$$H_b = \frac{(N_{FeedCH_4})(4)}{\left(N_{ProductH_2O}\right)(2) + \left(N_{ProductH_2}\right)(2) + (N_{ProductCH_4})(4)} \tag{7}$$

4. Conclusion

A series of precisely prepared Ni-Pt catalysts were prepared by electroless deposition and evaluated for the dry reforming of methane. When Pt is added to Ni nanoparticle surfaces via electroless deposition, a Ni rich alloy forms and the activity exhibits a maximum in Pt loading corresponding to 0.4 monolayers of Pt on Ni. Arrhenius data captured at low temperature conditions (525–600 °C) implies a synergistic effect on apparent activation energies corresponding to an increase in CH₄ conversion rates. At high temperature (700 °C) the nanoparticulate alloy phases segregated, in agreement with the bulk phase diagram. The resulting Pt rich ensembles promote methane activation to coke, the source of deactivation. In all cases Pt did had no effect on selectivity, which was instead driven by thermodynamic limits.

c Time on stream (hours).

Declaration of Competing Interest

The authors declare that they have no known competing financial interests or personal relationships that could have appeared to influence the work reported in this paper.

Acknowledgements

The authors would like to acknowledge the following NSF grant numbers IIP1464630, CBET1511615, and DGE1250052.

Appendix A. Supplementary material

Supplementary data to this article can be found online at https://doi.org/10.1016/j.jcat.2019.10.035.

References

- [1] I.M. Organization, The 2020 global sulphur limit (2018).
- [2] I.E. Agency, Tracking clean energy progress 2017 (2017).
- [3] D.o.M.R. North Dakota Industrial Commission, Oil and gas division, North Dakota Rules Regul. 304 (2017).
- [4] S. Afzal, D. Sengupta, A. Sarkar, M. El-Halwagi, N. Elbashir, Optimization approach to the reduction of CO2 emissions for syngas production involving dry reforming, ACS Sustain. Chem. Eng. 6 (2018) 7532–7544.
- [5] T.D. Gould, M.M. Montemore, A.M. Lubers, L.D. Ellis, A.W. Weimer, J.L. Falconer, W.J. Medlin, Enhanced dry reforming of methane on Ni and Ni-Pt catalysts synthesized by atomic layer deposition, Appl. Catal. A 492 (2015) 107–116.
- [6] C. Papadopoulou, H. Matralis, X. Verykios, Utilization of biogas as a renewable carbon source: dry reforming of methane, Catal. Alternat. Energy Generat. (2012) 71–141.
- [7] A.F. Lucrédio, J.M. Assaf, E.M. Assaf, Methane conversion reactions on Ni catalysts promoted with Rh: influence of support, Appl. Catal. A 400 (2011)
- [8] S.R.d. Miguel, I.M.J. Vilella, S.P. Maina, D.S. José-Alonso, M.C. Román-Martínez, M.J. Illán-Gómez, Influence of Pt addition to Ni catalysts on the catalytic performance for long term dry reforming of methane, Appl. Catal. A 435–436 (2012) 10–18.
- [9] K. Tomishige, S. Kanazawa, M. Sato, K. Ikushima, K. Kunimori, Catalyst design of Pt-modifoed Ni/Al203 catalyst with flat temperature profile methane reforming with CO2 and O2, Catal. Lett. 84 (2002) 69–74.
- [10] J.R. Rostrup-Nielsen, Sulfur-passivated nickel catalysts for carbon free steam reforming of methane, J. Catal. 85 (1984) 31–43.
- [11] S. Saadi, F. Abild-Pedersen, S. Helveg, J. Sehested, B. Hinnemann, C.C. Appel, J.K. Nørskov, On the role of metal step-edges in graphene growth, J. Phys. Chem. 114 (2010) 11221–11227.
- [12] S. Helveg, J. Sehested, J.R. Rostrup-Nielsen, Whisker carbon in perspective, Catal. Today 178 (2011) 42–46.
- [13] A.N. Şener, M.E. Günay, L. Aybüke, Y. Ramazan, Statistical review of dry reforming of methane literature using decision tree and artificial neural network analysis, Catal. Today 299 (2018) 289–302.
- [14] C.Y. Yuan, Y. Sheng, Sustainable scale-up studies of atomic layer deposition for microelectronics manufacturing, IEEE, 2010.
- [15] B.J. O'Neill, D.H.K. Jackson, L. Jechan, C. Canlas, P.C. Stair, C.L. Marshall, J.W. Elam, T.F. Kuech, J.A. Dumesic, G.W. Huber, Catalyst design with atomic layer deposition, ACS Catal. 5 (2015) 1804–1825.
- [16] B. Pawelec, S. Damyanova, K. Arishtirova, J.L.G. Fierro, L. Petrov, Structural and surface features of PtNi catalysts for reforming of methane with CO2, Appl. Catal. A 323 (2007) 188–201.
- [17] J. Tengco, B.T. Mehrabadi, Y. Zhang, A. Wongkaew, J. Regalbuto, J. Weidner, J. Monnier, Synthesis and electrochemical evaluation of carbon supported Pt-Co bimetallic catalysts prepared by electroless deposition and modified charge enhanced dry impregnation, Catalysts 6 (2016).
- [18] K. O'Connell, J.R. Regalbuto, High sensitivity silicon slit detectors for 1 nm powder XRD size detection limit, Catal. Lett. 145 (2015) 777–783.
- [19] M.F. Mark, W.F. Maier, CO2-Reforming of methane on supported Rh and Ir catalysts, J. Catal. 164 (1996) 122–130.

- [20] H. Jonathan, L. Catherine, L.E. C, A. Rose, S. Jason, Elucidating the impact of Ni and Co loading on the selectivity of bimetallic NiCo catalysts for dry reforming of methane, Chem. Eng. J. 352 (2018) 572–580.
- [21] M. Jabłońska, TPR study and catalytic performance of noble metals modified Al2O3, TiO2, and ZrO2 for low-temperature NH3 -SCO, Catal. Commun. 70 (2015) 66–71.
- [22] J.L. Ewbank, L. Kovarik, F.Z. Diallo, C. Sievers, Effect of metal-support interactions in Ni/Al2O3 catalysts with low metal loading for methane dry reforming, Appl. Catal. A 494 (2015) 57–67.
- [23] D. Fantauzzi, S.K. Calderon, J.E. Mueller, M. Grabau, C. Papp, H.P. Steinruck, T.P. Senftle, A.C.v. Duin, T. Jacob, Growth of stable surface oxides on Pt(111) at near-ambient pressures, Angew. Chem. Int. Ed. Engl. 56 (2017) 2594–2598.
- [24] N.W. Hurst, S.J. Gentry, A. Jones, B.D. McNicol, Temperature programmed reduction, Catal. Rev. 24 (1982) 233–309.
- [25] M.A.v. Spronsen, J.W.M. Frenken, I.M.N. Groot, Observing the oxidation of platinum, Nat. Commun. 8 (2017) 429.
- [26] W. Junmei, I. Enrique, Isotopic and kinetic assessment of the mechanism of reactions of CH4 with CO2 or H2O to form synthesis gas and carbon on nickel catalysts, J. Catal. 224 (2004) 370–383.
- [27] A.K. Ávetisov, J.R. Rostrup-Nielsen, V.L. Kuchaev, J.H.B. Hansen, A.G. Zyskin, E. N. Shapatina, Steady-state kinetics and mechanism of methane reforming with steam and carbon dioxide over Ni catalyst, J. Mol. Catal. A: Chem. 315 (2010) 155–162.
- [28] Z.L. Zhang, X.E. Verykios, Carbon dioxide reforming of methane to synthesis gas over supported Ni catalysts, Catal. Today 21 (1994) 589–595.
- [29] Z. Minhua, Y. Yingzhe, Z. Yongbo, DFT research of methane preliminary dissociation on aluminum catalyst, Appl. Surf. Sci. 280 (2013) 15–24.
- [30] M.C.J. Bradford, M.A. Vannice, CO2 reforming of CH4, Catal. Rev. 41 (1999) 1– 42.
- [31] M.C.J. Bradford, M.A. Vannice, Catalytic reforming of methane with carbon dioxide over nickel catalysts II. Reaction kinetics, Appl. Catal. A 142 (1996) 97– 122
- [32] E.L. Jablonski, A.A. Castro, O.A. Scelza, S.R.d. Miguel, Effect of Ga addition to Pt/Al2O3 on the activity, selectivity and deactivation in the propane dehydrogenation, Appl. Catal. A 183 (1999) 189–198.
- [33] S.A. Bocanegra, A.A. Castro, A. Guerrero-Ruíz, O.A. Scelza, S.R.d. Miguel, Characteristics of the metallic phase of Pt/Al2O3 and Na-doped Pt/Al2O3 catalysts for light paraffins dehydrogenation, Chem. Eng. J. 118 (2006) 161– 166
- [34] Z. Fulan, Z. Yujiao, X. Yihong, C. Guohui, W. Kemei, Effect of Si-doping on thermal stability and diesel oxidation activity of Pt supported porous γ-Al2O3 monolithic catalyst, Catal. Lett. 141 (2011) 1828–1837.
- [35] A.M. Robinson, M.M. Montemore, S.A. Tenney, P. Sutter, W.J. Medlin, Interactions of Hydrogen, CO, Oxygen, and Water with Molybdenum-Modified Pt(111), J. Phys. Chem. C 117 (2013) 26716–26724.
- [36] M.S. Hofman, Y. Yuxin, L. Wei, Y. Xiaofang, G.C. Schatz, B.E. Koel, Hydrogenation of CO on Ni(110) by energetic deuterium, J. Phys. Chem. C 122 (2018) 14671–14677.
- [37] T.D. Gould, A.M. Lubers, B.T. Neltner, J.V. Carrier, A.W. Weimer, J.L. Falconer, W. J. Medlin, Synthesis of supported Ni catalysts by atomic layer deposition, J. Catal. 303 (2013) 9–15.
- [38] H. Okamoto, Ni-Pt (Nickel-Platinum), J. Phase Equilib. Diffus. 31 (2010) 322-322.
- [39] L.A. Schulz, L.C.S. Kahle, K.H. Delgado, S.A. Schunk, A. Jentys, O. Deutschmann, J. A. Lercher, On the coke deposition in dry reforming of methane at elevated pressures, Appl. Catal. A 504 (2015) 599–607.
- [40] G.C. Bond, R.C. Francisco, E.L. Short, Kinetics of hydrolysis of carbon tetrachloride by acidic solids, Appl. Catal. A 329 (2007) 46–57.
- [41] G.C. Bond, M.A. Keane, H. Kral, J.A. Lercher, Compensation phenomena in heterogeneous catalysis: general principles and a possible explanation, Catal. Rev. 42 (2000) 323–383.
- [42] M. Williams, B. Fonfe, C. Woltz, A. Jentys, J. Vanveen, J. Lercher, Hydrogenation of tetralin on silica-alumina-supported Pt catalysts II. Influence of the support on catalytic activity, J. Catal. 251 (2007) 497–506.
- [43] R.C. Baetzold, G.A. Somorjai, Preexponential factors in surface reactions, J. Catal. 45 (1976) 94–105.
- [44] V.P. Zhdanov, J. Pavlicek, Z. Knor, Pre-exponential factors for elementary surface processes, Catal. Rev. 30 (1988) 501–517.
- [45] W. Linert, The isokinetic relationship, Chem. Soc. Rev. 18 (1989) 477–505.
- [46] O. Exner, Concerning the isokinetic relationship, Nature 201 (1964) 488-490.